ROYAL SOCIETY
OF CHEMISTRY

PAPER

Check for updates

Bulk charge-transfer coupling and tunable dielectric relaxation in benzoquinone-doped nematic liquid crystals

Yosr Turki, [ID] *[a] Bochra Bejaoui,[a] Ali Benali, [ID] [a] Mohamed Mastouri, [ID] [b] Noureddine Raouafi [ID] [b] and Youssef Arfaoui [ID] [c]

Developing next-generation electro-optic devices demands precise control over the dielectric dynamics of soft materials. To address this challenge, we report a systematic investigation of the nematic liquid crystal (LC) Merck IV doped with 1,4-benzoquinone (BQ) as a redox-active modulator. Through a combination of calorimetry, optical spectroscopy, and broadband impedance spectroscopy, rigorously analyzed *via* the electric modulus formalism, we identify a sharp concentration-dependent crossover between localized charge-transfer (CT) coupling and disorder-driven relaxation. Crucially, polarized optical microscopy confirms the preservation of the nematic phase across the explored concentration range. We find that at 1 wt%, BQ functions as an energetic modulator: it facilitates CT interactions that drastically lower the activation barrier for hopping conduction (~ 0.025 eV), although this comes with a slight increase in relaxation time due to steric constraints. This behavior highlights a critical trade-off where thermodynamic efficiency improves even as dipolar reorientation kinetically slows down. Conversely, increasing the load to 2 wt% shifts the system into a disorder-dominated regime. Here, π-stacked aggregates form deep traps and trigger Maxwell–Wagner–Sillars (MWS) interfacial polarization. Such disorder appears as a dynamic broadening of the relaxation spectrum, characteristic of charge transport within a rugged energy landscape. By demonstrating a decoupling between fast electronic transport and slow molecular reorientation, this study establishes BQ as a versatile, non-destructive dopant suitable for developing tunable dielectric LC materials.

1 Introduction

Mesophases known as liquid crystals (LCs) occupy an intermediate state of matter between the ordered nature of crystalline solids and the fluidity of isotropic liquids.[1] This hybrid character gives LCs structural adaptability and the ability to host and stabilize molecular guests. They remain responsive to temperature changes and applied electric fields. These properties account for their long-standing technological relevance, especially in liquid-crystal displays (LCDs), where controlled dielectric and optical anisotropies are required.[2] Beyond

conventional display applications, charge-transfer (CT) control in doped LCs may support new organic electronic devices and tunable electro-optical filters.

LC systems are typically classified as thermotropic phases, driven mainly by temperature, and lyotropic phases, which depend on solvent concentration.[3] Among thermotropic mesophases, the nematic phase plays a central role because of its structural simplicity, characterized by long-range orientational order without translational periodicity. This combination produces marked dielectric anisotropy, making nematic LCs well suited for studying polarization and dielectric relaxation.

The host matrix used for this investigation is *para*-butyl-*para*'-methoxyazoxybenzene, commercially known as Merck IV (M4), a well-established thermotropic nematic LC (NLC). M4 exhibits strong temperature sensitivity due to its conformational flexibility. As shown by Candau *et al.* in ultrasonic relaxation experiments,[4] this flexibility arises from both isomerization of the azoxy core and rotational motion of the terminal alkyl chains, which together provide several internal degrees of freedom. These motions, in turn, affect intermolecular interactions and collective dynamics; consequently,

[a] Functional Materials and Interfaces Group, Laboratory of Nanostructured Materials, Quantum and Nonlinear Optics, Department of Physics, Faculty of Sciences, University of Tunis El Manar, Tunis 2092, Tunisia. E-mail: yosr.turki@fst.utm.tn

[b] Sensors and Biosensors Group, Laboratory of Analytical Chemistry and Electrochemistry, Department of Chemistry, Faculty of Sciences, University of Tunis El Manar, Tunis 2092, Tunisia

[c] Laboratory of Characterizations, Applications and Modeling of Materials, Department of Chemistry, Faculty of Sciences, University of Tunis El Manar, Tunis 2092, Tunisia

macroscopic physical properties such as dielectric anisotropy and viscosity are highly dependent on the nematic order parameter.[5–7] Although M4 contains an azoxybenzene moiety capable of trans–cis photoisomerization, all dielectric measurements reported here were performed under strict dark conditions to exclude photoinduced artifacts from analysis.

Molecular doping provides an effective route to tuning the physical properties of nematic LCs; however, the choice of dopant is critical to avoid disruption of the mesophase. Quinones, particularly 1,4-benzoquinone (BQ), are well known for their redox activity and their ability to mediate CT interactions in organic systems.[8] Quinone-based motifs have also been reported to participate in liquid-crystalline self-assembly, suggesting that they can be incorporated into ordered soft-matter environments without necessarily compromising mesophase stability.[9–11] In contrast, stronger electron acceptors or ionic CT complexes, such as those based on tetracyanoquinodimethane (TCNQ), are known to induce rigid or anomalous mesophases that disrupt nematic order.[12] Beyond liquid-crystalline systems, BQ has also been employed as a mild redox-active molecule in advanced physicochemical contexts, further illustrating its versatile CT capability.[13]

Despite this potential, systematic investigations of low-weight-percentage BQ doping in conventional nematic hosts remain scarce. The present work addresses this gap. We investigate BQ concentrations of 0, 1 and 2 wt%, chosen to probe the regime from dilute doping up to 2 wt%, ensuring the maintenance of the nematic phase integrity as confirmed by polarized optical microscopy (POM). Dopant species significantly influence dielectric relaxation processes by modifying molecular alignment, dipolar interactions, and local structural organization. Comparable sensitivity has been observed in bimesogenic systems containing rod-like and bent-core mesogens,[14] providing a relevant framework for interpreting our results.

To guarantee robustness, we fabricated three LC cells (LCCs) and characterized them via impedance spectroscopy (IS), maintaining repeatability within 1%. Following multiscale physical characterization, we present a comprehensive dielectric analysis. We focus on thermally activated phenomena to show that dopant concentration allows for fine-tuning of bulk CT coupling and relaxation dynamics, providing a full picture of the interplay between molecular conformation and macroscopic performance.

2 Materials

2.1 Nematic host: Merck IV (M4)

Para-butyl-*para*'-Methoxyazoxybenzene, also marketed as Merck IV (M4),[15] is the nematic host used throughout this investigation. The molecule has an azoxybenzene core with butyl and methoxy tails on either side, as shown in Fig. 1(a) and (b). M4 exhibits a stable nematic mesophase in the approximate 289–349 K range.[4]

A defining characteristic of M4 is the reversible isomerization of its azoxy core. The rod-like *trans*-planar conformation
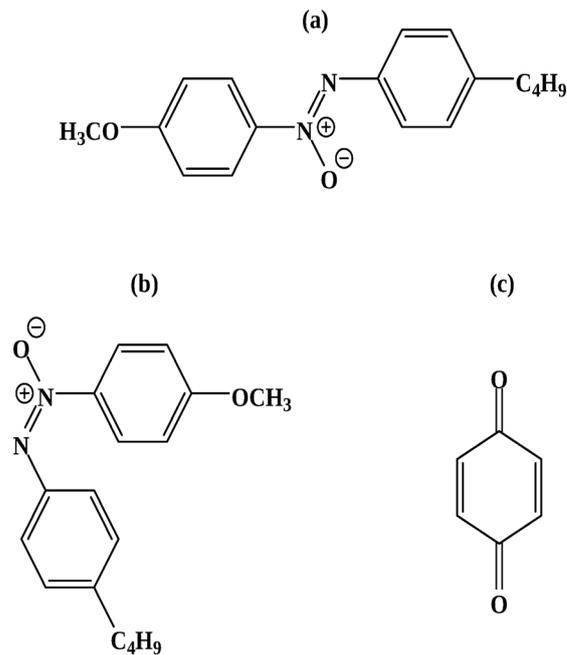

Fig. 1 Molecular architecture of the host-dopant system. (a) The rod-like *trans*-isomer of M4 (shown as a representative regioisomer of the eutectic mixture), which sustains the anisotropic nematic potential. (b) The bent *cis*-conformer, acting as a steric defect driven by thermal fluctuations or CT coupling. (c) 1,4-Benzoquinone (BQ), the planar redox-active acceptor responsible for electronic modulation.

stabilizes the nematic order (Fig. 1a), whereas the bent *cis* non-planar geometry (Fig. 1b) acts as a conformational impurity that locally disrupts mesophase alignment.[4,5] This conformational flexibility, coupled with rotational motion of the terminal chains, makes the dielectric and optical properties highly sensitive to temperature and external perturbations. Such sensitivity underpins the pronounced effect that dopants can exert on the mesophase organization.

2.2 Dopant: 1,4-benzoquinone (BQ)

1,4-Benzoquinone ($C_6H_4O_2$, BQ), the dopant, acts as a classical electron-accepting unit. Fig. 1c illustrates that BQ is a planar π-conjugated molecule with alternating C=C, C=O, and C-C bonds. Due to its strong electron affinity, it can interact effectively with the electron-rich LC host through donor–acceptor complex formation and π–π stacking.[16,17]

Beyond its intrinsic planarity, BQ exhibits significant redox versatility. The semiquinone radical anion ($C_6H_4O_2^{\bullet-}$), which extends π-electron delocalization across the ring, can be formed by its reversible acceptance of an electron in reaction to the local environment or thermal fluctuations. Small conformational or vibrational changes may have an impact on intermolecular interactions inside the LC matrix, supporting the ability of BQ to modulate the dielectric landscape.

To maintain BQ in its solid state (sublimation onset ≈ 366 K),[18] all experiments were carried out between 298 and 363 K, guaranteeing constant dopant concentrations throughout dielectric measurements. M4 and BQ were acquired from Sigma-Aldrich and utilized without additional purification.

3 Experimental methods

3.1 Sample preparation and cell fabrication

NLC cells were assembled from two FTO-coated glass substrates, unidirectionally rubbed to induce homogeneous planar alignment with zero pretilt. The substrates were bonded using a thermally stable adhesive, yielding a cell gap of $d \simeq 3.5$ μm and an active area of $S \simeq 2.25$ cm^2.

M4 was doped with BQ at concentrations of 1 and 2 wt% by mixing in the isotropic phase to ensure uniform distribution. Higher BQ concentrations (>2 wt%) led to sample inhomogeneity and loss of reproducible dielectric response, preventing reliable modulus analysis. A reference sample of pure M4 was also prepared. Capillary action was used to introduce the mixtures into the cells. Strict protocols were followed during all procedures, resulting in experimental repeatability among produced batches within a 1% margin.

3.2 Thermal and spectroscopic characterization

Phase transition behavior was analyzed using Differential Scanning Calorimetry (DSC, Shimadzu DSC-60A Plus). Samples were sealed in aluminum pans and subjected to heating and cooling cycles at rates of 5 K min^{-1} and 1 K min^{-1}, respectively, under a nitrogen purge (50 mL min^{-1}).

Optical absorption spectra were recorded in the 250–2000 nm range using a PerkinElmer Lambda 950 spectrophotometer. Vibrational properties were probed by Raman spectroscopy (Jobin Yvon HR LabRAM) in a backscattering confocal configuration, utilizing a 488 nm Ar$^+$ laser excitation. POM coupled with a Moticam camera allowed for the visual monitoring of mesophase textures and homogeneity during thermal cycles.

3.3 Broadband impedance spectroscopy

For dielectric characterization, we employed a PalmSens4 impedance analyzer in conjunction with a Linkam LTS420E-P thermal stage. The stage was electrically shielded and equipped with gold-plated tungsten probes to minimize external noise. The temperature was precisely controlled using a T96 controller with a ±0.01 °C accuracy.

Impedance spectra were acquired over the frequency range 0.1 Hz to 1 MHz using a sinusoidal excitation of $V_{AC} = 250$ mV with zero DC bias. This amplitude was particularly chosen to maximize the signal-to-noise ratio while ensuring the applied field remained below the threshold for field-induced reorientation (Freedericksz transition).[15] The counter (CE) and reference (RE) leads were shorted for the symmetric two-electrode setup (FTO–NLC–FTO) measurements. According to standard IS protocols, this configuration enables the reliable extraction of dielectric characteristics.[19,20] Data acquisition and analysis were performed using the PSTrace software package.

4 Results and discussion

4.1 Thermal behavior and phase transitions (DSC)

DSC was used to examine how BQ doping affected the thermal behavior and mesophase stability of M4. Fig. 2 displays representative thermograms for the endothermic and exothermic transitions, and Table 1 shows the collected thermodynamic parameters.

The thermal profile of the pristine sample reveals a distinct endothermic transition at 345.76 K ($\Delta H = +0.106$ J g^{-1}) immediately followed by an exothermic event at 347.28 K ($\Delta H = -0.082$ J g^{-1}). Although most nematic systems display a single clearing endotherm at T_{NI}, the presence of this double thermal feature is compatible with the intricate relaxation kinetics of the azoxybenzene moiety. As reported by Aronzon *et al.*[7] and De Jeu,[21] the transition is accompanied by a cooperative conformational reorganization. The exothermic contribution is commonly ascribed to the fast thermally driven relaxation of the *cis*-isomer fraction formed during the approach to the isotropic phase, which releases conformational strain energy stored in the disordered state. The close proximity of these transitions is indicative of cooperative mesogenic behavior where
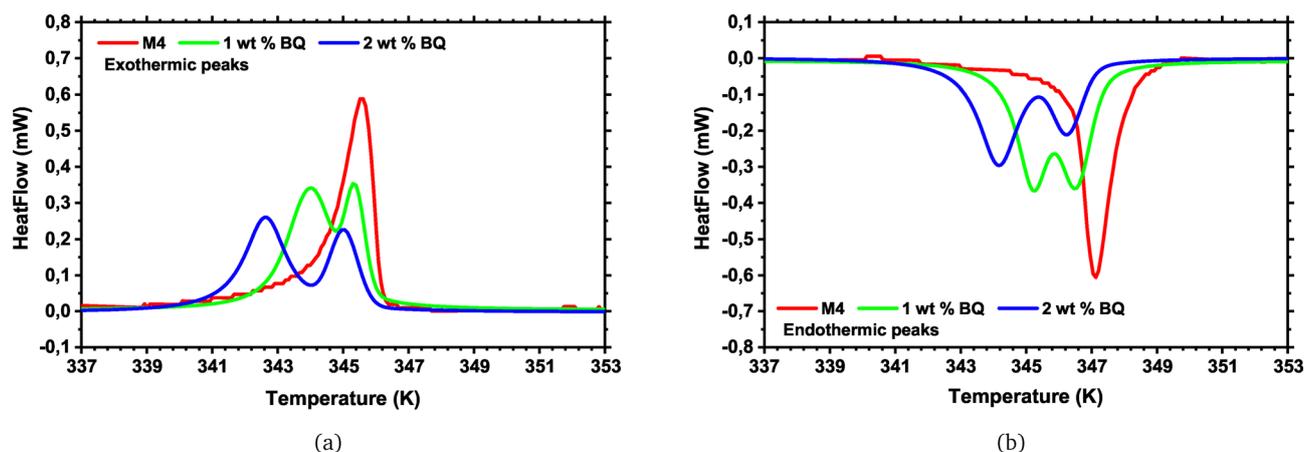

(a)

(b)

Fig. 2 Calorimetric mapping of the phase transition dynamics for (a) exothermic and (b) endothermic heat flows. The thermal profiles reveal a distinct evolution: the 1 wt% sample exhibits discrete peak splitting, signaling localized domain formation, whereas the 2 wt% sample undergoes diffusive thermal broadening. This evolution reflects a progressive increase in mesoscopic disorder.

Table 1 Thermodynamic parameters of phase transitions derived from DSC analysis. The quantitative evolution of transition temperatures, enthalpies (ΔH), and peak widths (FWHM) substantiates the crossover from discrete domain formation (1 wt%) to disorder-dominated broadening (2 wt%)

BQ (wt%)	Transition type	T (K)	ΔH (J g^{-1})	FWHM (K)
0%	Endo	345.76	+0.106	1.13
	Exo	347.28	−0.082	1.08
1%	Endo	344.13	+0.117	1.67
	Endo	345.54	+0.053	0.70
	Exo	345.36	−0.123	1.23
	Exo	346.69	−0.096	1.06
2%	Endo	342.74	+0.046	1.55
	Endo	345.2	+0.001	0.98
	Exo	344.3	−0.061	1.48
	Exo	346.43	−0.012	1.02

conformational fluctuations occur rapidly without disrupting the long-range order until the clearing point.

Upon doping with 1 wt% BQ, the thermal profile evolves, showing a clear splitting of both endothermic and exothermic transitions into satellite peaks (Fig. 2). The retention of the main transitions near 345.54 K and 346.69 K indicates that the bulk nematic order is preserved. However, the emergence of secondary peaks points to the formation of localized domains in which BQ induces specific dopant-host interactions. Rather than disrupt the nematic order, low-concentration BQ acts merely as a local source of perturbation, triggering partial isomerization while preserving the bulk mesophase stability.

At 2 wt% BQ, the discrete peak splitting disappears, replaced by a significant broadening of the transitions (increased FWHM) and a reduction in the endothermic enthalpy to +0.046 J g^{-1}. This diffuse thermal signature reflects a loss of cooperative behavior and the onset of structural heterogeneity. This pattern signals that the dopant load has breached the matrix's solubility threshold. Instead of providing local structural modulation, BQ behaves here as a macroscopic perturbation that progressively compromises mesophase cooperativity. This transition, from discrete peak splitting at 1 wt% to broadening at 2 wt%, is consistent with a crossover from localized perturbation to widespread structural disorder.

These thermal perturbations have direct implications for the material's functional properties. Since the dielectric anisotropy of M4 is governed by the conformational fluctuations of the azoxybenzene core,[21] the dopant-induced domains at 1 wt% are expected to modulate the local dipole moments *via* dipole–dipole coupling and π-stacking. Conversely, the loss of cooperativity at 2 wt% suggests a degradation of the net orientational order. To elucidate the molecular origin of these thermal shifts, specifically the role of CT interactions, we turn to optical and vibrational spectroscopy.

Complementing this thermal analysis, Fig. 3 follows the morphological evolution of the mesophase from the stable nematic range (333 K) to the isotropic transition. At 333 K, all samples display a continuous Schlieren texture with mobile disclinations, ruling out any macroscopic crystallization or phase separation. However, the optical contrast varies significantly: the dark appearance at 1 wt% BQ reflects the absorption of dispersed CT complexes, whereas the restored transmittance at 2 wt% supports the segregation of dopants into nanoscale aggregates. Upon heating to the clearing point, the texture evolves into a biphasic state where isotropic droplets nucleate within the nematic continuum (Fig. 3, bottom row). This coexistence of ordered ($S \neq 0$) and disordered ($S = 0$) phases provides direct visual evidence of the first-order nature of the transition, in full agreement with the Landau–de Gennes theory.[22] Crucially, the transition temperatures determined by POM mirror the DSC trend: T_{NI} decreases from 348 K (M4) to 346 K (1 wt%) due to the impurity effect, before anomalously recovering to 347.4 K at 2 wt%. This thermal rebound confirms that at higher loading, BQ molecules self-assemble into aggregates, thereby reducing the concentration of molecularly dispersed perturbations and allowing the bulk mesophase stability to recover towards that of the pristine host.

4.2 Electronic and conformational analysis (UV-VIS-NIR)

Optical absorption spectroscopy was used to probe the electronic interactions between the dopant and the matrix. As detailed in Table 2 and Fig. 4, the pristine M4 profile is anchored by a dual signature: a high-energy aromatic $\pi \rightarrow \pi^{\star}$ peak at 304.7 nm and a broad azoxy $n \rightarrow \pi^{\star}$ band centered at 398.9 nm. These spectral fingerprints confirm the extended conjugation inherent to the stable, rod-like *trans*-planar isomer.

Doping with 1 wt% BQ leads to the emergence of a new band at ∼331 nm, consistent with a partial *trans*-to-*cis* conformational change, as suggested by Aronzon *et al.*[7] Simultaneously, the main $n \rightarrow \pi^{\star}$ band undergoes a bathochromic shift to 407.4 nm, indicating a modification of the electronic environment driven by donor–acceptor CT interactions.

Increasing the BQ loading to 2 wt% induces a significant spectral reorganization. The main band undergoes a hypsochromic (blue) shift to 397.4 nm accompanied by a marked narrowing of the linewidth, as quantified in Table 2 (FWHM contracts from 26.5 nm to 14.0 nm). According to excitonic coupling models for molecular aggregates, such a blue shift coupled with spectral narrowing is the characteristic signature of H-aggregates, resulting from the parallel alignment of transition dipoles in face-to-face π-stacked assemblies.[23,24] Concurrently, the suppression of the *cis*-band signal indicates a shift in interaction dynamics: at this density, the dopant preferentially self-assembles into stacked domains rather than coupling individually with the LC host.

4.3 Vibrational fingerprinting (Raman spectroscopy)

We verified the conformational evolution, as suggested by UV-VIS, using Raman spectroscopy. Fig. 5 illustrates how the vibrational landscape shifts under increasing BQ loads. The pristine host signal is notably rigid, effectively capturing the thermodynamic stability of the *trans*-planar geometry. The signature is dominated by the intense mode at 1242.6 cm^{-1},
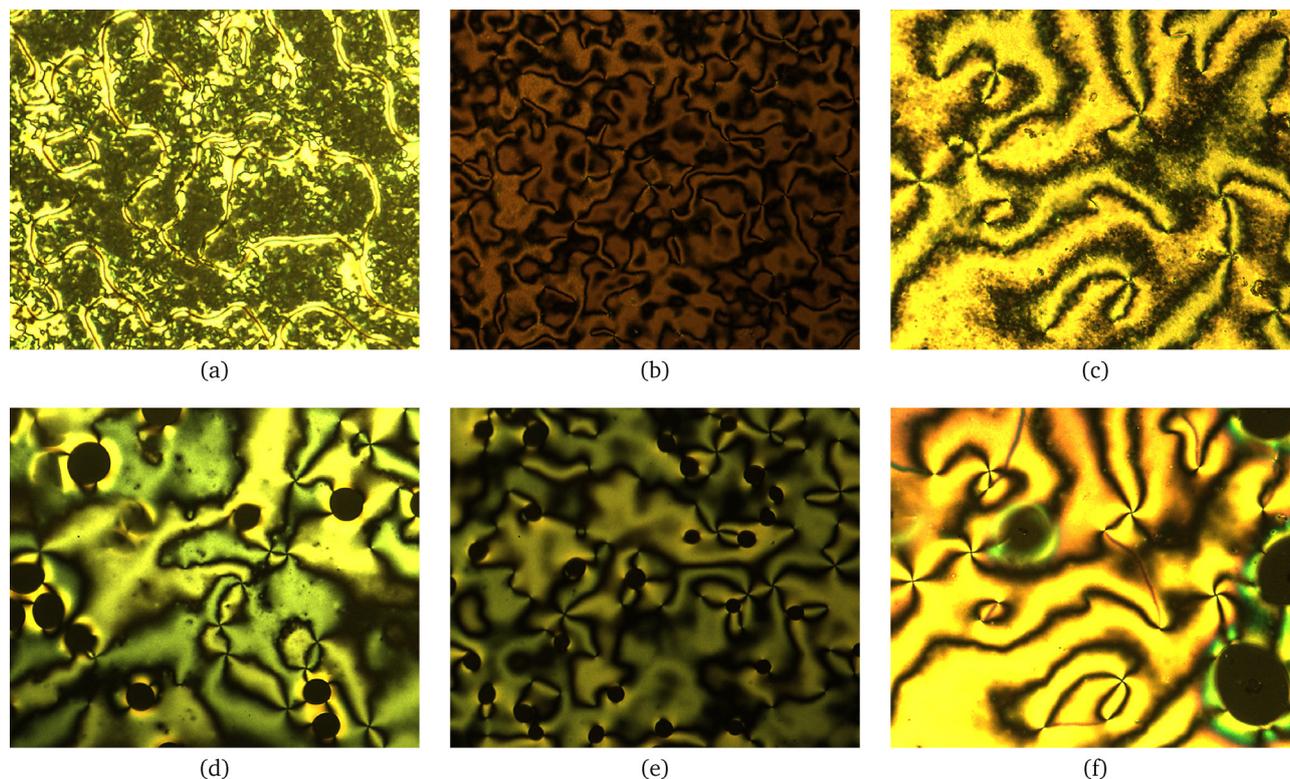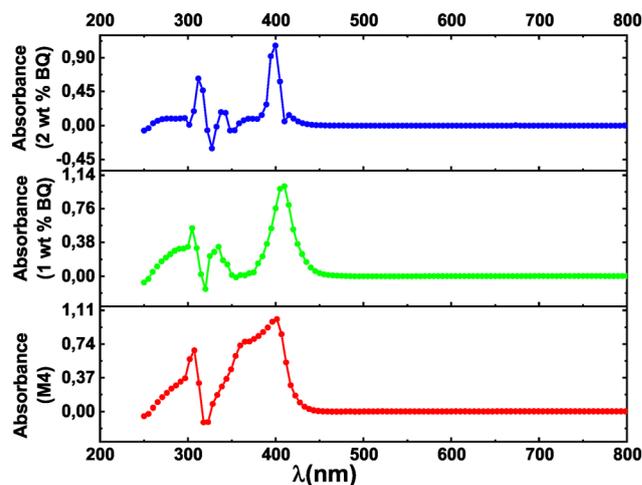
Fig. 3 Polarized optical microscopy (POM) textures under crossed polarizers. Top row: Textures at 333 K for (a) M4, (b) 1 wt% BQ, and (c) 2 wt% BQ, showing stable nematic Schlieren domains. The darker contrast in (b) reflects homogeneous CT interactions, while the recovery of transmittance in (c) suggests dopant segregation. Bottom row: Coexistence of nematic and isotropic phases near T_{NI} for (d) M4 ($T \approx 348$ K), (e) 1 wt% BQ ($T \approx 346$ K), and (f) 2 wt% BQ ($T \approx 347.4$ K). The biphasic region confirms the first-order nature of the transition consistent with Landau–de Gennes theory.

Table 2 Quantitative optical descriptors tracking the crossover in electronic coupling. At 1 wt%, the bathochromic shift and spectral broadening (see $\pi \rightarrow \pi^*$ FWHM) highlight disorder induced by individual donor–acceptor interactions. In sharp contrast, the 2 wt% regime is governed by a hypsochromic shift and spectral contraction, quantifying the locking of the dopant into supramolecular H-aggregates

BQ (wt%)	Band	λ_{max} (nm)	Absorbance (a.u.)	FWHM (nm)
0%	1st	304.7	0.62	19.4
	2nd	398.9	1.00	61.7
1%	1st	305.5	0.52	27.9
	2nd	331.2	0.29	17.6
	3rd	407.4	1.00	26.5
2%	1st	314.6	0.54	10.4
	2nd	340.5	0.17	9.3
	3rd	397.4	1.00	14.0
	4th	421.3	0.09	12.5

Fig. 4 UV-VIS-NIR absorption spectra of the pristine and BQ-doped M4 systems. The plots reveal the electronic signature of supramolecular reorganization. At 1 wt%, the emergence of the $\sim$331 nm band captures the dopant-induced *trans*-to-*cis* isomerization. Conversely, the 2 wt% spectrum is governed by a hypsochromic shift and significant spectral narrowing, definitive fingerprints of H-type aggregation (face-to-face π-stacking) that dominates over individual molecular coupling.

assigned to the asymmetric stretching of the azoxy linkage (N═N → O) coupled with aromatic skeletal vibrations. Additional markers at 1433.5 cm^{-1} ($\nu_{C═C}$) and 1361.4 cm^{-1} (ν_{C-N}) confirm the extensive conjugation and planarity of the mesogenic core.[25,26] No modes characteristic of distorted or *cis*-geometries are detectable in the undoped state.

Upon doping with 1 wt% BQ, the vibrational environment is significantly perturbed, reflecting the symmetry breaking observed in thermal and optical data. A new band emerges at

1042.4 cm^{-1}, corresponding to the C–O stretching vibration of the methoxy tail. The sensitivity of this mode to doping

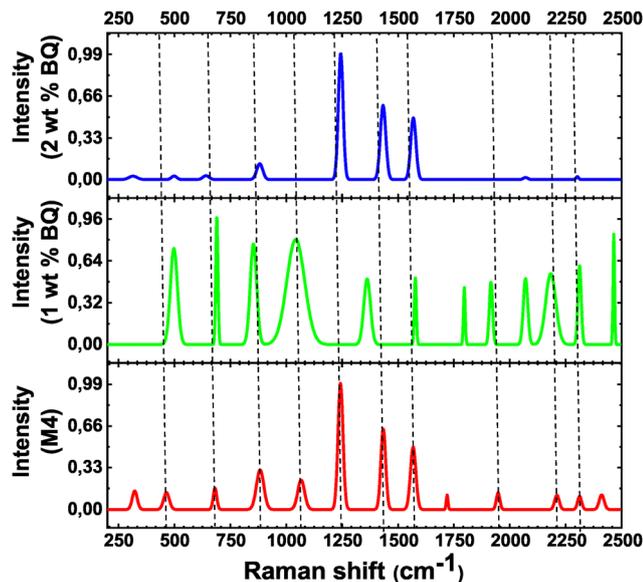**Fig. 5** Raman spectra showing the vibrational fingerprinting of the conformational evolution. The emergence of the CT-specific mode (1042.4 cm^{-1}) and twist-related markers (688.6 cm^{-1}) at 1 wt% reveals a dopant-induced symmetry breaking. At 2 wt%, the suppression of these signatures confirms dopant segregation: BQ aggregation prevents local coupling, effectively restoring the bulk *trans*-planar spectral profile.

indicates a specific CT interaction between the electron-deficient BQ and the electron-rich alkoxy donor sites of the host.[27] Concurrently, the spectrum develops distinct markers at 688.6 cm^{-1} (aromatic ring twisting) and 853.8 cm^{-1} (out-of-plane C–H deformation), signaling a clear loss of planarity. In light of recent computational benchmarks for azobenzene derivatives,[28,29] we assign these signatures to twisted intermediate or *cis*-isomeric states. This provides spectroscopic evidence that, at low concentrations, BQ exerts a local torque, driving the twisting of the azoxy core.

At 2 wt% BQ, the spectrum exhibits a counter-intuitive structural recovery. The CT-specific band at 1042.4 cm^{-1} disappears, and the twist-related modes at 688.6 cm^{-1} are no longer detectable. The spectrum largely reverts to the *trans*-dominated signature, with the 1244.9 cm^{-1} band intensity restored. Additionally, new low-intensity modes emerge at 497.6 and 641.9 cm^{-1}, likely arising from aggregate-specific skeletal modes within the formed clusters. This observation indicates that at higher concentrations, BQ molecules preferentially self-associate into aggregates rather than interacting individually with the LC matrix. According to the theory of molecular aggregation,[24,30] such self-association disrupts local donor–acceptor coupling. Consequently, the vibrational signature mimics the pristine host not because of a macroscopic structural recovery, but due to dopant segregation: the aggregates no longer individually perturb the host matrix locally, leading to a spectrum dominated by the bulk *trans*-isomer signal despite the global disorder observed in DSC. This spectroscopic evidence aligns closely with the blue shift (H-aggregation) observed in UV-VIS spectra and the loss of thermal cooperativity measured by DSC.

5 Electrical and dielectric properties

5.1 Analytical framework: the electric modulus

Based on the structural and morphological observations of nanoscale aggregation and local disorder established above, this section investigates the effects of BQ doping on charge transport and relaxation dynamics in the nematic host, with particular emphasis on bulk processes revealed through electric modulus analysis. Dielectric measurements were performed using IS over a broad frequency range (0.1 Hz–1 MHz).[31,32] While IS typically provides the complex impedance $Z^*(\omega) = Z'(\omega) - jZ''(\omega)$, the analysis of doped LCs is often complicated by the superposition of electrode polarization, ionic conduction, and dipolar relaxation.

In such disordered systems, particularly where dopant segregation induces hopping conduction and interfacial heterogeneity, standard equivalent-circuit models (*e.g.*, Randles–Ershler or simple RC circuits) frequently yield non-unique or physically ambiguous parameters.[33,34] Consequently, we avoid arbitrary circuit fitting and instead adopt the electric modulus formalism (M^*) as the primary analytical tool.

Originally proposed by McCrum[35] and further developed by Macedo,[36] this formalism is conceptually analogous to the mechanical modulus in viscoelasticity, as discussed in early anelastic and dielectric analyses of polymeric solids.[37] Its key advantage lies in its ability to minimize electrode polarization effects, which dominate the permittivity ε^* at low frequencies, and to resolve bulk relaxation processes even in the presence of significant DC conductivity.[38,39] This approach, historically effective for ion-conducting polymers,[40] has recently been validated for disentangling conduction pathways from intrinsic relaxation in complex doped systems.[41–43]

The real (M') and imaginary (M'') components of the electric modulus are derived directly from the measured impedance Z^* using the standard interconversion relations established for electroceramics and disordered systems:[31,44,45]

$$M'(\omega) = \frac{\varepsilon'}{(\varepsilon')^2 + (\varepsilon'')^2} = -\omega C_0 Z''(\omega) \qquad (1)$$

$$M''(\omega) = \frac{\varepsilon''}{(\varepsilon')^2 + (\varepsilon'')^2} = \omega C_0 Z'(\omega) \qquad (2)$$

where ε' and ε'' form the complex permittivity ε^*, and $C_0 = \varepsilon_0 S/d$ is the vacuum capacitance of the empty cell. This direct transformation allows us to bypass the explicit calculation of permittivity, thereby filtering out the electrode polarization that typically obscures low-frequency data in the ε^* domain.

In this representation, maxima in $M''(\omega)$ correspond to characteristic relaxation times of mobile charge carriers, enabling a direct identification of bulk transport and relaxation dynamics.

5.2 Dielectric relaxation context

The theoretical basis for dielectric relaxation in nematic systems is well established. Near the glass transition or in the presence of dopants, the distinction between conductivity and

dipolar relaxation becomes intricate.[46] As noted by De Jeu,[5,21] the dielectric response of azoxybenzenes is sensitive to both molecular rotation and conformational fluctuations.

In our BQ-doped system, the raw impedance spectra are dominated by resistive pathways at low frequencies, a signature of strong electrode polarization effects.[47] By converting to the modulus representation (M^*), we effectively filter out these extrinsic contributions. This allows for a coherent separation of interfacial polarization from intrinsic dipolar reorientation, revealing clear temperature- and concentration-dependent features that distinguish the pristine homogeneous host from the structurally perturbed BQ-doped systems.

5.3   Charge transport and impedance analysis (Z')

To quantify the resistive footprint of the dielectric response, we tracked the real impedance component, $Z'(\omega)$ (Fig. 6). In the low-frequency band ($F < 10^2$ Hz), the signal is governed by long-range ionic drift and electrode polarization. Consistent with thermally activated transport, heating the sample drastically cuts Z', mirroring the surge in ionic mobility. Yet, doping imposes a distinct resistive increase: at any given isotherm, the magnitude of Z' scales with BQ load. This effect becomes conspicuous at 2 wt%, where impedance remains elevated even at high temperatures. We attribute this hindrance to the formation of BQ aggregates that function as deep charge traps, effectively limiting free carrier density and impeding long-range ionic migration.[34,48]

Spanning 10^2 to 10^4 Hz, the intermediate frequency band bridges the gap between ionic conduction and bulk dielectric relaxation. Unlike the pristine host, which displays a sharp step-like transition, the BQ-doped samples show a progressively smeared dispersion zone. We interpret this spectral broadening as a departure from homogeneous Debye dynamics toward a distribution of relaxation times, the hallmark of a disordered dielectric environment where local dipoles encounter heterogeneous electrostatic constraints.

At high frequencies ($F > 10^4$ Hz), where dipolar relaxation dominates, a temperature-dependent inversion is observed, particularly for the undoped and 1 wt% samples. While heating reduces Z' at low frequencies (facilitating conduction), it leads to a slight increase in Z' in the high-frequency region. This behavior arises from the thermally activated shift of the dielectric relaxation peak toward higher frequencies. Thermal activation drives the relaxation peak into the measurement window, where dielectric losses project onto the real impedance axis, raising the resistive baseline well above the frozen state.[32] The scenario changes drastically at 2 wt%: here, the system remains locked in a state of anomalously high impedance across the entire bandwidth. This provides clear evidence that dopant aggregates act as persistent barriers, simultaneously hindering ionic drift and cooperative dipolar rotation.

5.4   Dielectric permittivity response (ε^*)

We map the raw polarization landscape *via* the complex permittivity, $\varepsilon^* = \varepsilon' - j\varepsilon''$ (Fig. 7), initially capturing the system's response prior to suppressing extrinsic contributions. Below 10^2 Hz, the real component ε' climbs steeply. This parasitic divergence signals strong electrode polarization and space-charge buildup at the LC/FTO boundaries.[32,47] A parallel feature dominates the imaginary spectrum ε'': a sharp $1/\omega$-type ascent indicative of dominant DC conductivity and ionic dissipation.[34] Heating the system amplifies these extrinsic signals, driven by the thermal mobilization of both ionic impurities and dopant-generated carriers.

Increasing the BQ load visibly alters the landscape: the low-frequency ε' plateau scales up while the high-frequency dispersion broadens. We attribute this to heightened dynamic disorder, where BQ molecules function as charge traps, leading to the formation of micro-environments characterized by distributed relaxation times.[41] In the raw permittivity data, pronounced extrinsic signals mask the intrinsic dipolar response, rendering the extraction of the characteristic relaxation time τ *via* ε^* unreliable.[39] Consequently, the electric modulus formalism (M^*) is adopted to isolate bulk relaxation processes. By filtering out interfacial artifacts and damping the DC conductivity contribution, M^* enables access to the intrinsic dipolar relaxation dynamics.[36] The M'' peaks, in particular, provide a clean metric to resolve the characteristic relaxation frequency and its thermal shift, allowing for a rigorous
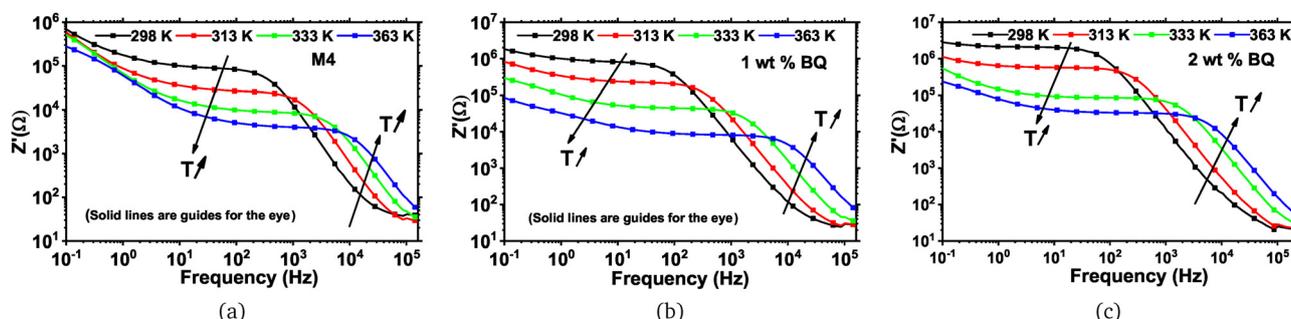

Fig. 6   Frequency dispersion of the resistive component Z' at representative temperatures for (a) the pristine host, (b) 1 wt% BQ, and (c) 2 wt% BQ. The low-frequency plateau maps the ionic conduction baseline, which scales up with dopant load due to charge trapping. At high frequencies, the steep drop signals the crossover to bulk dielectric relaxation. The complete dataset covering the full thermal range (14 isotherms from 298 K to 363 K, $\Delta T = 5$ K) is provided in Fig. S1 of the SI. Solid lines are guides to the eye.
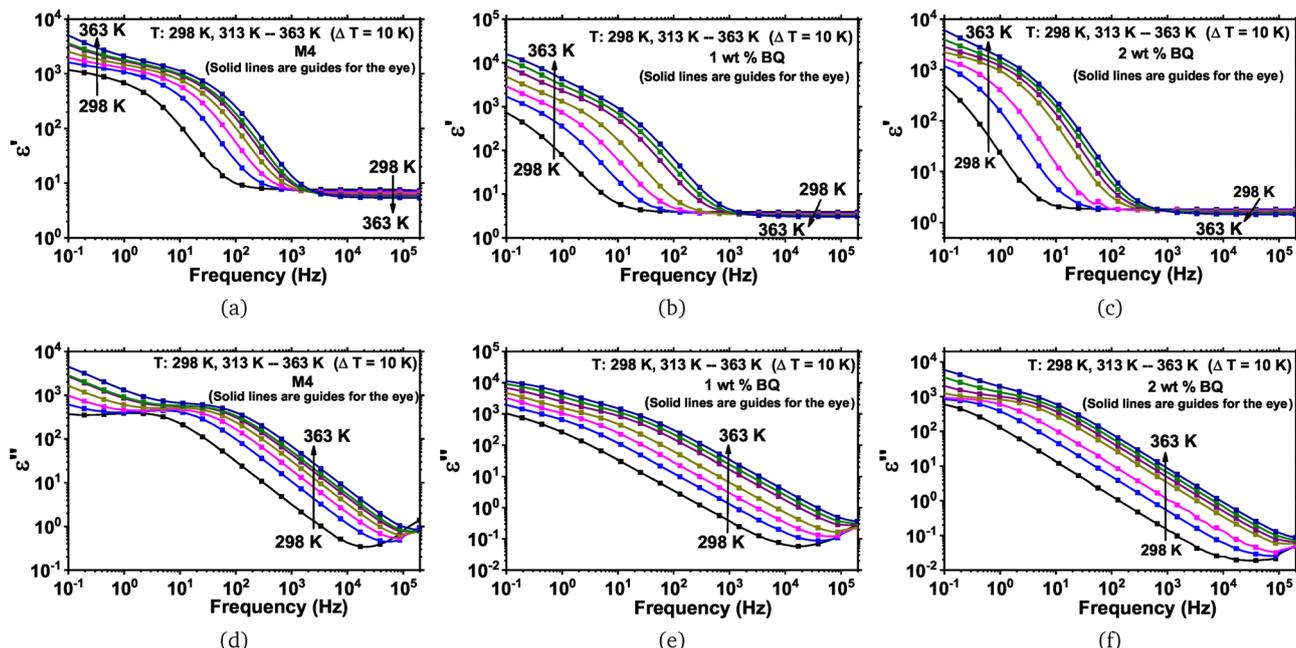
Fig. 7 Frequency dispersion of the real (ε', top row) and imaginary (ε'', bottom row) permittivity for the pristine host, 1 wt% BQ, and 2 wt% BQ-doped systems. The steep low-frequency divergence reflects parasitic electrode polarization and space-charge accumulation at the interfaces, which mask the intrinsic dipolar response and motivate the use of the electric modulus formalism for bulk analysis. For clarity, only selected isotherms are displayed here ($\Delta T = 10$ K), with a reduced data-point density. The complete dataset covering the full thermal range (298–363 K, $\Delta T = 5$ K) is provided in Fig. S2 of the SI. Solid lines are guides to the eye. Plots (a) and (d) correspond to the M4 host; plots (b) and (e) to the 1 wt% BQ system; and plots (c) and (f) to the 2 wt% BQ system.

quantification of how BQ reshapes both orientational dynamics and localized conduction.

5.5 Real part of electric modulus (M')

Fig. 8(a)–(c) show the frequency-dependent evolution of the real part of the electric modulus M' for the three LCC systems over the 298–363 K range. A clear transition is observed between two regimes, separated by a characteristic inflection frequency ($F_{\text{inflection}}$). At low frequencies ($\simeq 0.1$–10 Hz), M' approaches a quasi-static value close to zero. This vanishing behavior illustrates the efficacy of the modulus formalism: it effectively suppresses the electrode polarization contribution allowing for the resolution of bulk processes.[36] In this region, dielectric

relaxation is overshadowed by ionic drift, as mobile charges readily follow the slowly varying electric field, and M' decreases with temperature due to the thermally activated screening of interfacial polarization.

Above $F_{\text{inflection}}$, M' increases with frequency and rises further with temperature, reflecting the progressive involvement of dipolar units and localized charge carriers within the LC matrix contributing to the polarization process. At high frequencies ($> 10^4$ Hz), M' reaches a plateau, M'_∞, associated with the full participation of dipoles and short-range carriers in the dielectric response. This dispersion marks the transition from long-range ionic drift to short-range polarization processes. As temperature increases, this dispersion step shifts
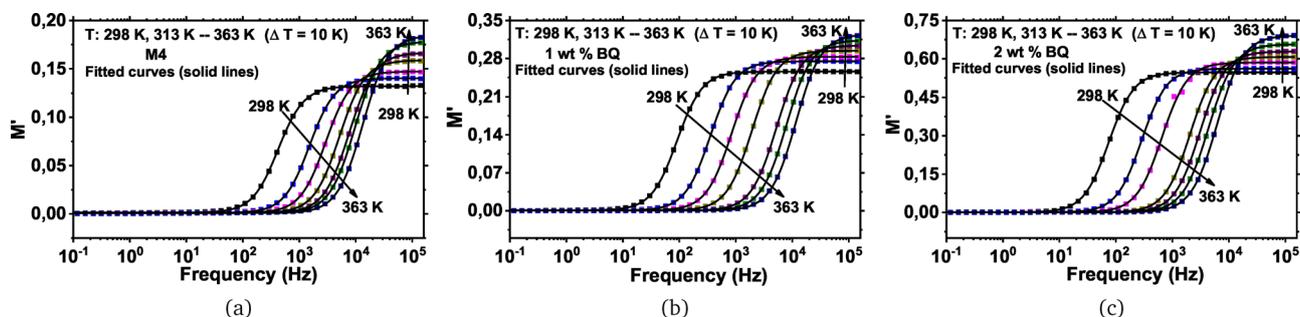

Fig. 8 Frequency dispersion of the real electric modulus M' at representative temperatures for (a) the pristine host M4, (b) 1 wt% BQ, and (c) 2 wt% BQ-doped samples. The inflection frequency, $F_{\text{inflection}}$, marks the kinetic crossover: the low-frequency vanishing of M' reflects interfacial screening, while the high-frequency rise signals the thermal activation of intrinsic bulk dipolar relaxation. The complete dataset covering the full thermal range (14 isotherms 298–363 K) is provided in Fig. S3 of the SI.

toward higher frequencies, confirming the thermal activation of the underlying dipolar relaxation. Accordingly, the value of $F_{inflection}$ serves as a robust marker for separating interfacial phenomena from intrinsic bulk polarization.

The functional form of $M'(F)$ allows for quantitative fitting using a modified sigmoidal equation:

$$M'(F) = M'_\infty + \frac{\Delta M'}{1 + \left(\frac{F}{F_{inflection}}\right)^p}, \qquad (3)$$

with

$$\Delta M' = M'_\infty - M'_s. \qquad (4)$$

The exponent p quantifies the sharpness of the transition and is typically close to 2 in this study. The relatively abrupt increase in M' around $F_{inflection}$ reflects the homogeneous nature of the dominant relaxation processes in the undoped and lightly doped samples, whereas the progressively broader transitions observed at higher BQ content indicate the emergence of distributed relaxation dynamics.

Quantitatively, at 333 K, the undoped M4 sample displays a gradual rise from near-zero values at 0.1 Hz to $\simeq 0.159$ at 100 kHz, characterized by an inflection modulus $M'_{inflection} \simeq 0.08$ at 5.13 kHz. At the same temperature, the 1 wt% BQ-doped system exhibits a steeper ascent ($M' \simeq 0.294$ at 100 kHz) and a higher inflection modulus ($M'_{inflection} \simeq 0.147$ at 1.92 kHz), indicating enhanced dipolar dynamics. For 2 wt% BQ, the increase becomes even more pronounced ($M' \simeq 0.61$ at 100 kHz), with $M'_{inflection} \simeq 0.304$ occurring at 2.04 kHz. The broadening of the dispersion slope observed at this concentration signals a wider distribution of relaxation times and a departure from Debye behavior.

For all compositions, $F_{inflection}$ shifts toward higher frequencies as temperature increases, a signature of thermally activated dipolar relaxation. At a fixed temperature, the dependence on BQ concentration reveals a non-monotonic behavior, most notably near 333 K, where a clear deviation from Arrhenius behavior. This anomaly corresponds to a specific kinetic crossover documented in the relaxation time analysis, where the 2 wt% sample paradoxically exhibits faster dynamics ($\tau \approx 7.80 \times 10^{-5}$ s) than the 1 wt% sample ($\tau \approx 8.27 \times 10^{-5}$ s). We attribute this anomaly to the thermal destabilization of the BQ

H-aggregates identified by UV-VIS spectroscopy. Since these supramolecular assemblies are stabilized by non-covalent π–π stacking interactions,[24] the thermal energy at 333 K ($k_B T \approx 0.028$ eV) becomes sufficient to shift the equilibrium towards partial dissociation. This thermal release of charge carriers from deep aggregate-induced traps effectively reduces the effective energetic disorder width σ within the framework of the Gaussian Disorder Model.[49] Consequently, transport pathways that were previously hindered by steric effects and trapping are progressively restored.

Overall, the evolution of $M'(F)$ reflects a transition from intrinsic dipolar relaxation mechanisms to more spatially heterogeneous relaxation processes, driven by dopant-induced perturbations in the bulk organization of the LCC matrix.

The internal consistency of this analysis is verified by examining the spectral overlay presented in Fig. 9. In an ideal Debye system, the frequency at which the imaginary component $M''(F)$ reaches its maximum coincides exactly with the inflection point of the real part $M'(F)$. Our experimental data exhibit this precise frequency coincidence, thereby providing strong support for the physical validity of the electric modulus formalism applied in the present study.[50]

5.6 Imaginary part of the electric modulus (M'')

The imaginary modulus, M'', serves as a rigorous gauge for energy dissipation. It explicitly tracks the kinetic lag of dipoles and mobile charge carriers driven by the oscillating field. Unlike the dielectric loss ε'', which is often obscured by electrode polarization and DC conductivity, the M'' formalism suppresses such extrinsic contributions, thereby isolating the intrinsic relaxation dynamics of the material.[51] The resulting frequency-dependent peak in M'' marks the characteristic relaxation frequency of the system, where the phase lag between the driving field and molecular reorientation is maximized.

Fig. 10 shows the evolution of M'' for temperatures ranging from 298 K to 363 K. For all samples, the relaxation peak shifts systematically toward higher frequencies with increasing temperature, reflecting a thermally activated hopping process. However, the doping effect reveals a complex interplay between energetics and sterics.
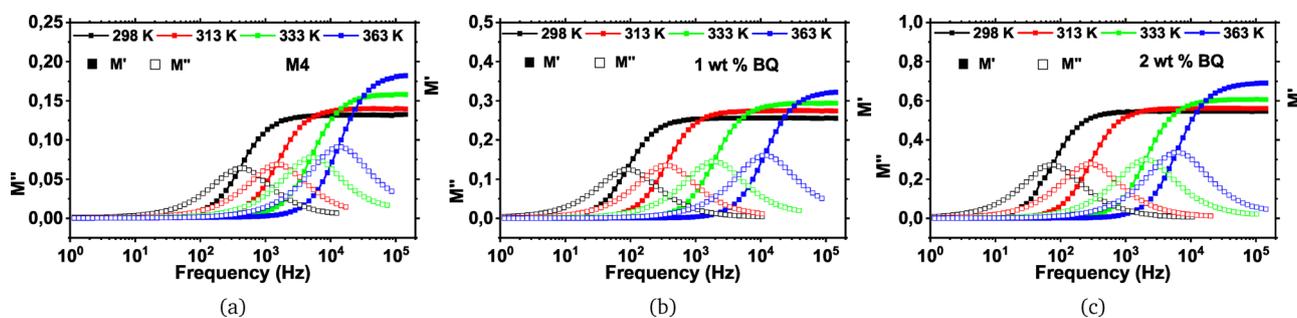

Fig. 9 Internal consistency validation of the modulus formalism. The strict frequency alignment between the M' inflection point and the M'' loss peak confirms the physical fidelity of the relaxation analysis. Plots correspond to (a) pure M4, (b) 1 wt% BQ, and (c) 2 wt% BQ-doped samples.
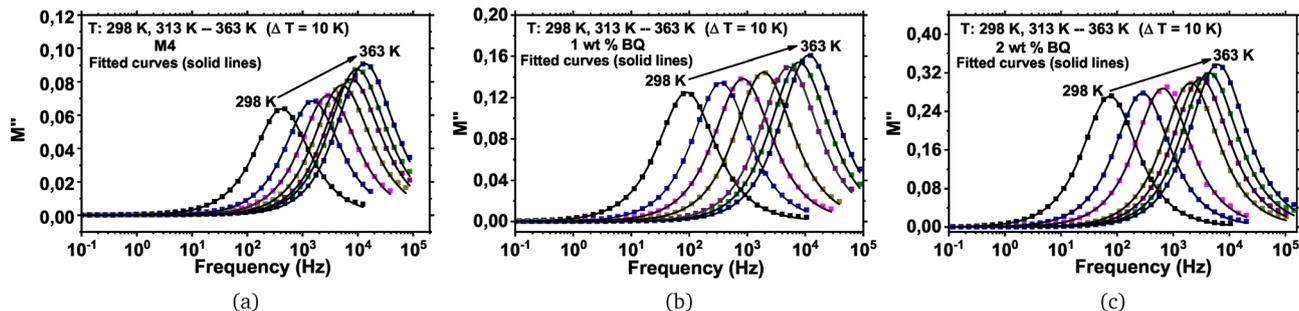
Fig. 10 Frequency evolution of the imaginary electric modulus M'' at representative temperatures for (a) the pristine host M4, (b) 1 wt% BQ, and (c) 2 wt% BQ-doped samples. The systematic peak shift tracks the thermal activation kinetics of dipolar reorientation. Simultaneously, the broadening observed in (c) maps the onset of dynamic heterogeneity, reflecting a departure from ideal Debye behavior driven by the rugged energetic landscape of the aggregated phase. The complete dataset covering the full thermal range (14 isotherms, 298–363 K) is provided in Fig. S4 of the SI. Solid lines represent the best fits using the generalized Bergman function.

Quantitatively, the relaxation frequency for the undoped M4 host increases from $\sim$421 Hz at 298 K to $\sim$13.3 kHz at 363 K. In the 1 wt% BQ-doped sample, the peak is shifted to significantly lower frequencies, ranging from $\sim$91 Hz to $\sim$11.5 kHz over the same interval. When converted to relaxation time τ (see Table 4), this corresponds to an increase from 3.78×10^{-4} s (undoped) to 1.76×10^{-3} s (1 wt% BQ) at 298 K. This significant slowing ($\sim$4.5$\times$) contradicts a simple lubricating effect and highlights that while BQ facilitates CT, its bulky structure introduces steric hindrance that decelerates the global dipolar reorientation.

In contrast, the 2 wt% BQ sample exhibits a peak at even lower frequencies (from $\sim$75 Hz to $\sim$6.2 kHz) together with visible broadening. At 298 K, this corresponds to a relaxation time $\tau \simeq 2.13 \times 10^{-3}$ s. This behavior points to dopant-induced structural heterogeneity and localized trapping, consistent with the aggregation model described in the structural analysis.

Activation energies extracted from $M''_{\max}$ follow an Arrhenius-type dependence and decrease from $\simeq$0.040 eV (undoped) to $\simeq$0.025 eV at 1 wt% BQ, before partially recovering to $\simeq$0.032 eV at 2 wt% BQ (Table 4). This reduction confirms that moderate doping facilitates local charge mobilization by lowering the energetic barrier, even though the global relaxation dynamics are kinetically slowed by steric constraints.

A notable feature of the undoped host is the sharp rise of M'' above 10^4 Hz at elevated temperatures, which indicates the emergence of a secondary, faster relaxation mode or short-range vibronic process entering the experimental frequency window. This contribution becomes less visible in doped samples, where the dominant ionic and localized polarization processes mask the intrinsic high-frequency tail.

To quantify the observed peak broadening and asymmetry, the M'' spectra were fitted using the generalized Bergman function, a phenomenological expression derived from the modified Kohlrausch–Williams–Watts (KWW) stretched-exponential model.[52–54] The imaginary modulus is expressed as:

$$M'' = \frac{M''_{\max}}{\frac{1-|a-b|}{a+b}\left[b\left(\frac{F_{\max}}{F}\right)^a + a\left(\frac{F}{F_{\max}}\right)^b\right] + |a-b|}. \quad (5)$$

The parameters a and b encode the asymmetry of the relaxation peak on the low- and high-frequency sides, respectively. When a, $b \to 1$, the relaxation approaches the ideal Debye limit with a single relaxation time. At lower temperatures, eqn (5) provides excellent fits for all systems.

The extracted parameters (Table 3) show that b is consistently slightly smaller than a for all samples and temperatures, indicating subtle deviations from Debye behavior on the high-frequency side of the peak. For the pristine host, the proximity of a and b to unity confirms a tightly focused distribution of relaxation times. Doping introduces a slight symmetry breaking: while the low-frequency slope retains its Debye character ($a \approx 1$), the high-frequency tail shows a minor elongation ($b \approx 1$), a distortion that maps the rise of dopant-induced heterogeneity.[55–57]

The simultaneous analysis of normalized impedance $-Z''$ and electric modulus M'' spectra offers further insight into the relaxation mechanisms. Fig. 11 displays these overlays at 298 K. In most cases, the peaks coincide, indicating that dipolar reorientation and short-range charge transport share a common relaxation time, consistent with a Debye-like response involving weak dispersion.

Table 3 Shape analysis of the relaxation spectrum *via* the generalized Bergman parameters. The proximity to unity ($a \approx b \approx 1$) confirms a quasi-Debye behavior, while the slight inequality ($b < a$) reveals a subtle high-frequency spectral stretching

	M4		1 wt% BQ		2 wt% BQ	
T (K)	a	b	a	b	a	b
298	0.98	0.96	0.97	0.97	1.00	0.98
303	1.00	0.96	0.98	0.97	1.00	0.98
308	1.00	0.96	0.98	0.97	0.99	0.98
313	1.00	0.96	0.98	0.97	1.00	0.97
318	1.00	0.95	0.99	0.97	0.99	1.00
323	1.00	0.95	1.00	0.96	1.00	0.97
328	1.00	0.94	1.00	0.95	1.00	0.97
333	1.00	0.93	1.00	0.95	1.00	0.96
338	1.00	0.93	1.00	0.95	1.00	0.96
343	1.00	0.93	1.00	0.95	1.00	0.95
348	1.00	0.93	1.00	0.95	1.00	0.95
353	1.00	0.93	1.00	0.94	1.00	0.95
358	1.00	0.92	1.00	0.94	1.00	0.94
363	1.00	0.93	1.00	0.94	1.00	0.94

Table 4 Evolution of the characteristic relaxation time τ extracted from modulus spectroscopy. The global increase in τ at 298 K reflects the steric load imposed by the dopant complexes. The specific crossover observed at 333 K marks the thermal dissociation of BQ aggregates, leading to a counter-intuitive recovery of mobility at higher concentrations

T (K)	M4	1 wt% BQ	2 wt% BQ
298	3.78×10^{-4}	1.76×10^{-3}	2.13×10^{-3}
303	2.34×10^{-4}	1.08×10^{-3}	1.40×10^{-3}
313	1.05×10^{-4}	4.50×10^{-4}	5.60×10^{-4}
323	5.43×10^{-5}	1.90×10^{-4}	2.44×10^{-4}
333	3.10×10^{-5}	8.27×10^{-5}	7.80×10^{-5}
343	2.08×10^{-5}	3.06×10^{-5}	5.17×10^{-5}
353	1.64×10^{-5}	2.03×10^{-5}	3.66×10^{-5}
363	1.19×10^{-5}	1.38×10^{-5}	2.56×10^{-5}

A subtle anomaly surfaces at 298 K for the 2 wt% load: the modulus and impedance peaks drift apart (Fig. 11c). We interpret this lag as a transient decoupling of local dipolar relaxation (dominated by M'') from long-range conduction ($-Z''$). Physically, this stems from charge trapping at defect sites or microdomains that bottleneck extended ionic motion without freezing local polarization. Thermal energy resolves this split; as heat releases trapped carriers, the two processes resynchronize. Such peak mismatch falls strictly within Gerhardt's interpretation, serving as a diagnostic for the coexistence of localized and extended relaxation pathways.[50,58]

5.7 Analysis of dielectric functions and activation energies

To probe the energetic landscape governing the dielectric response, we analyzed the thermal evolution of key parameters extracted from the electric modulus spectra: the relaxation strength $\Delta M'$, the inflection modulus $M'_{\text{inflection}}$, the peak loss modulus M''_{max} and the characteristic relaxation time $\tau = (2\pi F_{\text{max}})^{-1}$. Together, these metrics map the energy landscape restricting charge transport and molecular rotation. We modeled the thermal kinetics using the standard Arrhenius relation:

$$X(T) = X_0 \exp\left(-\frac{E_{\text{a}}}{k_{\text{B}}T}\right) \qquad (6)$$

where X_0 represents the pre-exponential factor and E_{a} the activation barrier against thermal energy $k_{\text{B}}T$. Table 5 compiles the activation energies derived from the linear regressions shown in Fig. 12–15.

A clear dynamical decoupling emerges when comparing the energetics of the modulus amplitudes $(\Delta M', M''_{\text{max}})$ versus the relaxation kinetics (τ). The amplitude parameters exhibit remarkably low activation energies ($E_{\text{a}} \sim 0.025$–0.040 eV), comparable to the thermal energy at room temperature ($k_{\text{B}}T \approx 0.026$ eV). These low barriers are characteristic of electronic hopping or the release of charge carriers from shallow traps.[31] The reduction of this barrier at 1 wt% BQ (~ 0.025 eV) confirms that moderate doping facilitates local charge mobilization.

In contrast, the relaxation time τ exhibits much higher activation energies ($E_{\text{a}} \sim 0.67$–0.75 eV), consistent with molecular reorientation processes, notably the trans-to-cis isomerization of the azoxybenzene core.[7] This disparity reveals a clear decoupling between fast, low-barrier charge-hopping processes and slower, cooperative structural rearrangements of the host
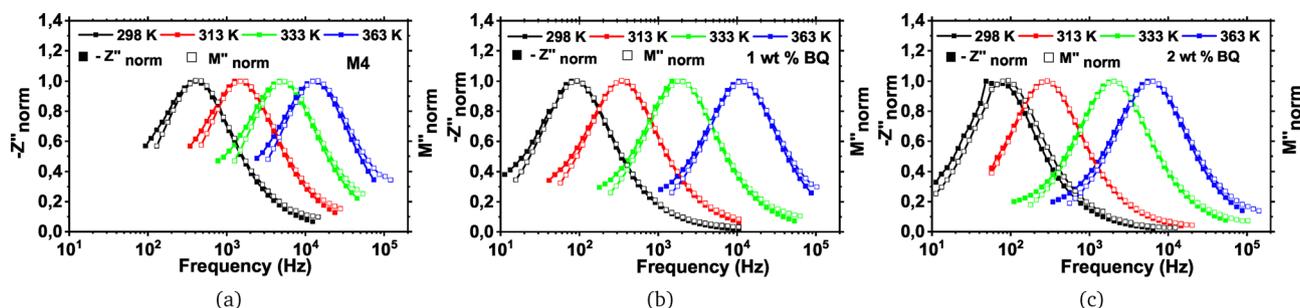
Fig. 11 Normalized spectral overlay of impedance ($-Z''$, solid symbols) and electric modulus (M'', open symbols) at representative temperatures for (a) undoped M4, (b) 1 wt% BQ, and (c) 2 wt% BQ-doped samples. Spectra are scaled to their maxima according to $-Z''_{\text{norm}} = -Z''/(-Z'')_{\text{max}}$ and $M''_{\text{norm}} = M''/M''_{\text{max}}$. In the pristine and 1 wt% samples, the perfect frequency coincidence of the peaks confirms that conduction and relaxation share the same timescale. In contrast, the 2 wt% sample (c) reveals a distinct peak shift (kinetic decoupling) at high temperatures, marking the transition to trap-controlled transport.

Table 5 Activation energies (E_{a}) derived from dielectric descriptors. The contrast between low amplitude energies (hopping) and high relaxation energies (isomerization) reflects the decoupling of transport and structure

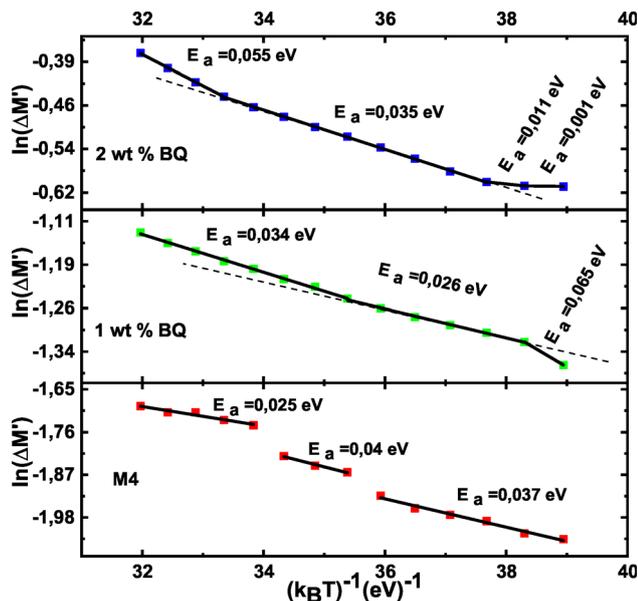|	M4		1 wt% BQ		2 wt% BQ	
Descriptor	Range (K)	E_{a} (eV)	Range (K)	E_{a} (eV)	Range (K)	E_{a} (eV)
$\Delta M'$	298–323	0.037 ± 0.002	303–328	0.026 ± 0.001	308–348	0.035 ± 0.001
$M'_{\text{inflection}}$	298–323	0.034 ± 0.002	303–328	0.025 ± 0.001	308–348	0.034 ± 0.001
M''_{max}	298–323	0.040 ± 0.002	303–328	0.025 ± 0.001	308–348	0.032 ± 0.001
τ	298–318	0.675 ± 0.010	298–333	0.747 ± 0.005	298–328	0.732 ± 0.007

Fig. 12 Arrhenius plot of the relaxation strength $\Delta M'$. The transition from the stepped profile of the undoped host to the continuous evolution in doped samples maps the onset of energetic disorder (Bässler/Dyre models).
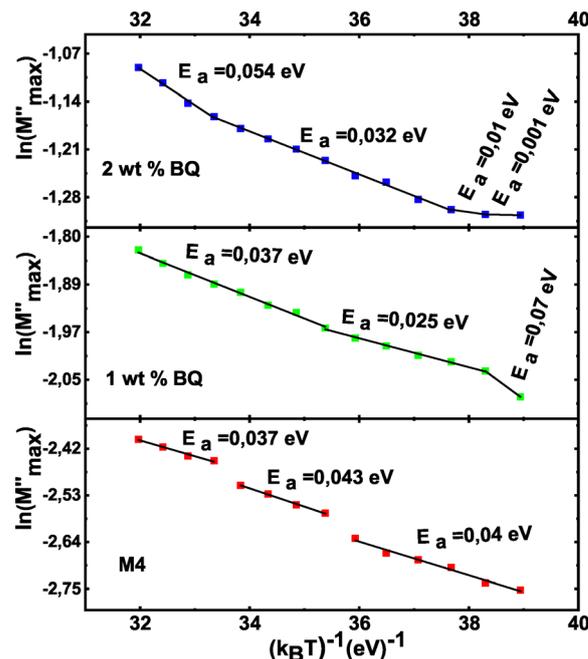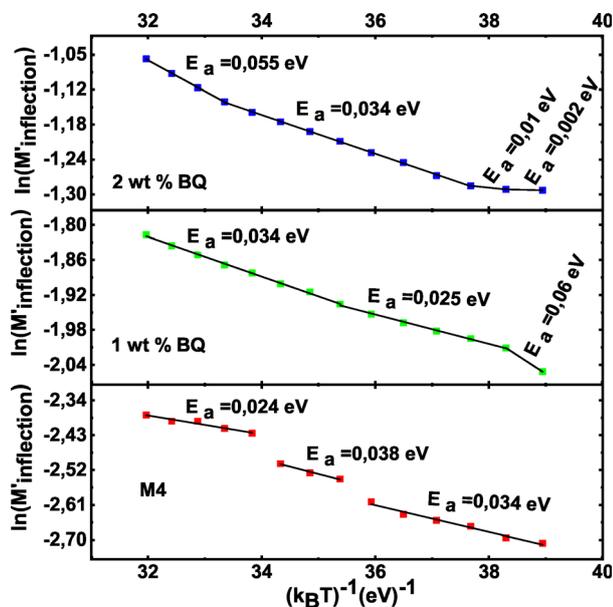

Fig. 13 Arrhenius plot of the inflection modulus $M'_{\text{inflection}}$. As a marker of the crossover from extrinsic to intrinsic polarization, its thermal dependence yields the activation energy (E_a) governing the onset of bulk relaxation.

Fig. 14 Arrhenius plot of the peak loss modulus M''_{max}. The low activation energies derived here (~ 0.025–0.040 eV) identify electronic hopping as the dominant transport mechanism, distinct from the slower molecular reorientation.

behaviour with three distinct linear regimes, which we attribute to the successive dominance of different relaxation pathways (local dipolar reorientation, cooperative molecular rearrangements, and thermally activated *trans–cis* isomerization). Upon introduction of BQ, these sharp slope changes are progressively smoothed into a continuous temperature dependence.

This smoothing is naturally rationalized by models of transport in disordered media. In the Gaussian disorder model (GDM) of Bässler,[49] the energetic positions of localized electronic states are described by a Gaussian distribution with width σ, and charge transport occurs *via* thermally assisted hops. As σ increases, the macroscopic response averages over many local environments, producing temperature dependence that deviates from a single Arrhenius law and varies continuously with T. Complementarily, Dyre's random free-energy barrier model[60] shows that a broad distribution of activation barriers yields frequency- and temperature-dependent responses governed by the statistics of these barriers rather than a single characteristic energy.

Physically, BQ (and its aggregates) introduces both energetic disorder (spread of site energies and trap depths) and structural heterogeneity (local distortions, micro-domains), so that charge carriers and local dipoles experience a rugged potential environment. Consequently, instead of sharp, system-wide reorganizations at specific temperatures, different micro-regions activate at different temperatures, and the experimentally observed activation energy becomes an effective, averaged quantity.[61] This picture accounts for the smoothing of Arrhenius plots, the reduction in amplitude-related activation energies at moderate doping, and the

matrix, including the *trans–cis* pathway. Such a separation of timescales is reminiscent of glass-forming systems, where localized charge motions remain partially decoupled from structural relaxation.[59]

The profile of the Arrhenius plots (Fig. 12) provides direct insight into how BQ doping reshapes the energetic environment of the nematic host. The pristine M4 shows a stepped Arrhenius
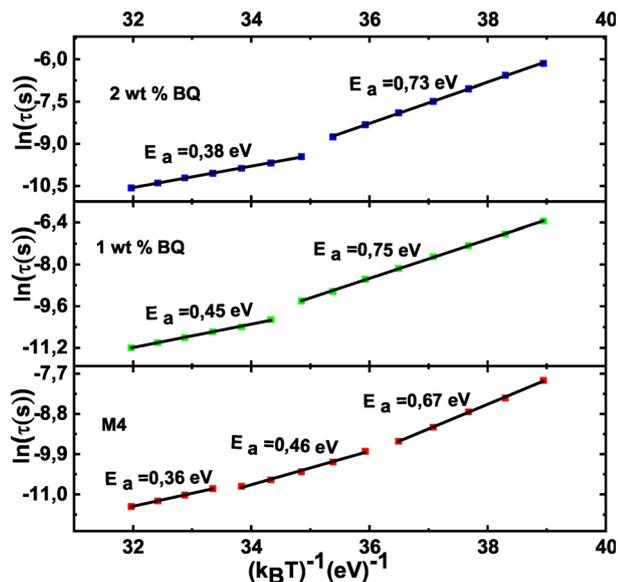
Fig. 15 Arrhenius plot of the characteristic relaxation time τ. The high activation barriers (~ 0.7 eV) identify molecular isomerization as the rate-limiting step, confirming the kinetic decoupling from the fast electronic hopping.

partial recovery of trapping behavior at higher loading due to aggregation, which creates deeper local traps.[49]

Quantitative analysis at 323 K shows that τ increases from 5.4×10^{-5} s in the undoped system to 1.9×10^{-4} s at 1 wt% BQ, and further to 2.4×10^{-4} s at 2 wt% BQ. Although doping slightly slows the global relaxation kinetics compared to the pristine host due to steric effects, the 1 wt% sample exhibits the lowest activation energies. This confirms that 1 wt% represents a thermodynamic optimum, minimizing the energetic cost of transport without the severe blocking effects observed at higher concentrations.

5.8 Dielectric loss and interfacial polarization (tan δ)

The dielectric loss tangent, defined as:

$$\tan \delta = \frac{\varepsilon''}{\varepsilon'} = \frac{M''}{M'} \qquad (7)$$

quantifies the fraction of stored electric energy dissipated during each field cycle. In nematic systems, $\tan \delta$ captures the combined action of bulk dipolar relaxation, ionic migration, and interfacial polarization, offering a macroscopic signature of the dissipation mechanisms active within the mesophase.[51]

Fig. 16 presents the frequency evolution of $\tan \delta$ between 298 and 363 K. A critical feature of these spectra is the non-coincidence between the $\tan \delta$ peak frequency and that of the intrinsic relaxation observed in M''. For the undoped M4 at 298 K, the $\tan \delta$ peak occurs at ~ 57 Hz, whereas the M'' maximum appears around 421 Hz. This frequency gap widens significantly with temperature (reaching 1.32 kHz $vs.$ 13.3 kHz at 363 K) and is consistently observed in all doped samples. For instance, in the 1 wt% BQ-doped system, the peaks shift from 5.86 Hz $vs.$ 90.6 Hz at 298 K to 475 Hz $vs.$ 11.5 kHz at 363 K.

This spectral mismatch is physically significant. Drawing on the criteria established by Sidebottom[59] and Gerhardt,[50,58] we interpret this lack of overlap as clear evidence that the driving processes have kinetically decoupled. The $\tan \delta$ peak is dominated by long-range ionic conduction and interfacial effects (lower frequencies), whereas M'' highlights localized dipolar relaxation (higher frequencies). The widening gap at elevated temperatures confirms that thermal activation accelerates bulk dipolar reorientation ($E_a \sim 0.7$ eV) much more effectively than collective ionic drift ($E_a \sim 0.03$ eV), consistent with the large disparity in their energetic barriers identified in the previous section.

At higher dopant loadings, the $\tan \delta$ response becomes noticeably distorted, with the effect being most pronounced for the 2 wt% BQ sample (Fig. 16c). The emergence of a strong low-frequency shoulder together with a broadened leading edge is characteristic of Maxwell–Wagner–Sillars (MWS) interfacial polarization.[61] Such features are expected when conductive or polar inclusions, here BQ aggregates, introduce internal interfaces where charge can accumulate under an AC field. Within the universal dielectric response (UDR) framework,[34] these spectral anomalies are naturally interpreted in terms of charge carriers undergoing trapping–detrapping at heterogeneous boundaries, thereby supporting the disorder-driven transport scenario inferred from the Arrhenius analysis.
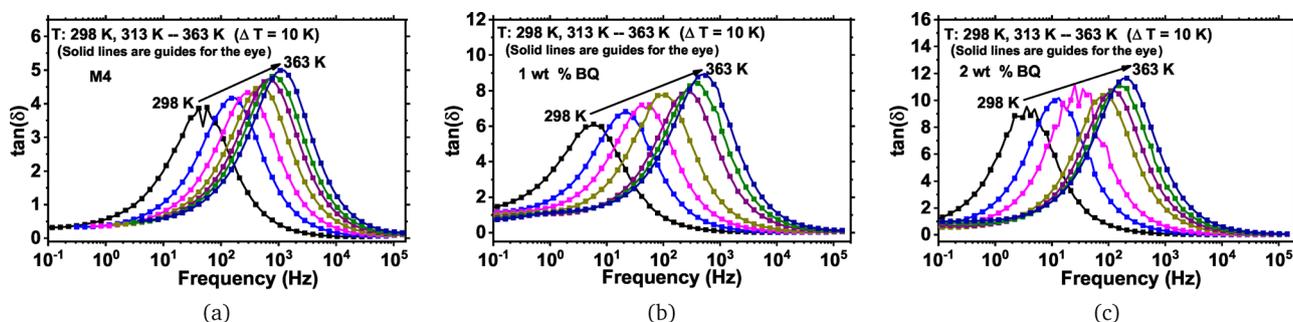

Fig. 16 Frequency evolution of the dielectric loss tangent ($\tan \delta$) at representative temperatures for (a) undoped M4, (b) 1 wt% BQ, and (c) 2 wt% BQ-doped samples. The distinct shift toward lower frequencies relative to the modulus peak (M'') confirms that low-frequency dissipation is dominated by ionic conduction. In the 2 wt% sample (c), the spectral distortion marks the onset of MWS interfacial polarization. The complete dataset covering the full thermal range (14 isotherms, 298–363 K) is provided in Fig. S5 of the SI. Solid lines act as guides for the eye.

Consequently, while tan δ serves as a sensitive diagnostic for interfacial heterogeneity and conduction phenomena, the electric modulus remains the superior formalism for resolving the intrinsic bulk dipolar dynamics of these complex nematic composites.

5.9 Topology of relaxation: Nyquist analysis of electric modulus

The Nyquist plots of the complex electric modulus (M'' vs. M'), shown in Fig. 17, provide a topological map of the relaxation processes. All systems exhibit well-defined semicircles, indicative of a dominant relaxation mechanism, yet their geometric evolution reveals progressive modifications in conduction and dipolar dynamics induced by BQ doping.

The semicircle radius (R_{Nyquist}) serves as a direct measure of the inverse capacitance ($M \propto \varepsilon^{-1}$). In the pure M4 host, R_{Nyquist} remains small and nearly constant (0.06 at 298 K to 0.09 at 363 K), reflecting a homogeneous intrinsic polarizability. With a 1 wt% BQ load, the semi-circle radius increases markedly ($0.12 \rightarrow 0.16$), and this trend escalates at 2 wt% ($0.27 \rightarrow 0.34$). Physically, this expansion of the modulus arc corresponds to a decrease in the effective capacitance. We attribute this to the blocking effect of BQ aggregates: rather than enhancing polarization, these clusters disrupt the continuity of the liquid crystalline matrix, acting as constrictions that hinder long-range charge displacement and reduce the bulk polarizability.[42,61]

Crucially, the semicircles are depressed below the M' axis. This depression is quantified by the angle θ (deviation from ideal Debye behavior where $\theta = 0$) and corresponds geometrically to the vertical displacement of the semicircle center (M''_{center}). Fig. 18 shows that $|\theta|$ exhibits non-monotonic thermal variations, strongly correlated with the fluctuations of M''_{center} (Fig. 19). Rather than experimental noise, these fluctuations reflect the sequential thermal activation of different relaxation channels within a rugged potential-energy landscape.[60]

The thermal evolution of the 2 wt% BQ sample reveals two distinct regimes. First, at low temperatures (298 K), the system exhibits an anomalously low depression angle ($\theta \approx 0.30°$),
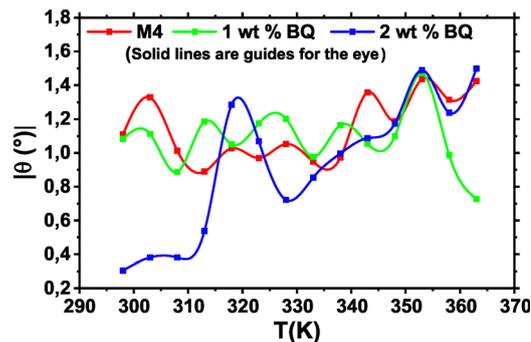

Fig. 18 Temperature dependence of the non-Debye depression angle $|\theta|$. The 2 wt% sample exhibits distinct fluctuations, contrasting with the stable host response. These fluctuations reflect dynamic heterogeneity, indicative of charge transport through a rugged energy landscape with distributed trap depths.

significantly lower than that of the pristine host ($\sim1.1°$). Contrary to the expectation that doping-induced disorder should broaden the relaxation time distribution, this quasi-Debye behavior indicates that charge carriers are confined by well-defined interfaces, specifically the boundaries of the BQ aggregates observed by POM. This confinement temporarily masks the intrinsic microscopic heterogeneity of the energetic landscape, triggering a MWS effect that mimics a simplified relaxation pathway.[61] Second, as temperature rises towards 333–353 K, θ increases sharply and fluctuates, reaching a plateau above 353 K. This signals the progressive activation of localized charge populations and the onset of defect-mediated transport. This interpretation aligns perfectly with the texture refinement observed by microscopy around 333 K (see Fig. 3), confirming that the dielectric landscape is modulated by the thermal dissociation of aggregates.

This behavior demonstrates that BQ doping does not merely act as a static source of disorder. Instead, it induces a dynamic heterogeneity:[62,63] the distribution of relaxation times fluctuates as thermal energy allows the system to explore different configurations of the energy landscape. Within the Dyre framework, these features are interpreted as thermally activated fluctuations between shallow and deep trapping configurations, rather than as evidence of a distinct thermodynamic
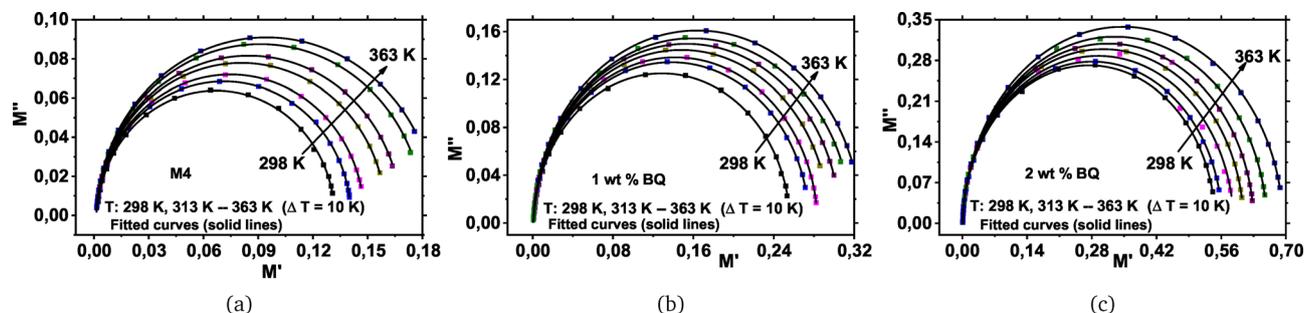

Fig. 17 Nyquist diagrams of the complex electric modulus (M'' vs. M') at representative temperatures for (a) undoped M4, (b) 1 wt% BQ, and (c) 2 wt% BQ-doped samples. The geometric expansion of the semicircles corresponds to a decrease in effective capacitance, identifying BQ aggregates as blocking micro-capacitors that hinder long-range transport. The complete dataset covering the full thermal range (14 isotherms, 298–363 K) is provided in Fig. S6 of the SI. Solid lines represent the best fits to semicircular arcs.
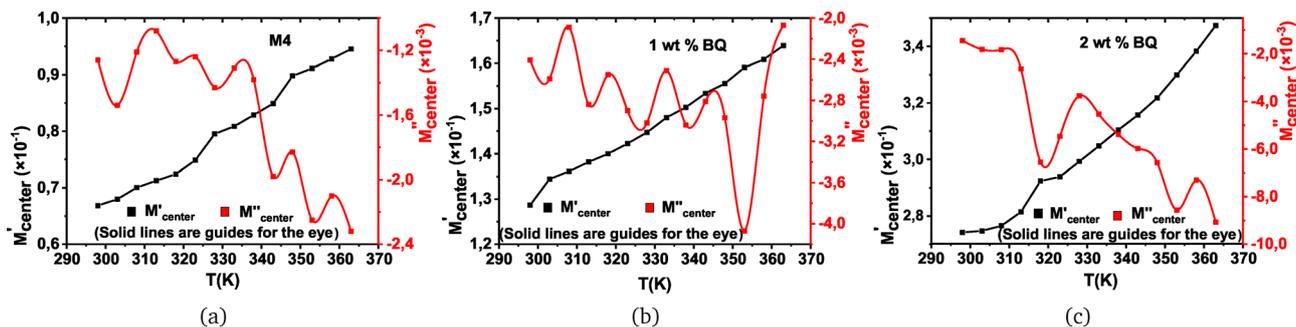
Fig. 19 Temperature evolution of the Nyquist semicircle center coordinates $(M'_{center}, M''_{center})$. The fluctuations in M''_{center} signal dynamic trapping/detrapping events, correlated with the variations in θ. (a), (b), and (c) correspond to the M4, 1 wt% BQ, and 2 wt% BQ samples, respectively.

phase transition. Quantitative analysis of the center coordinates further supports this picture. While M'_{center} increases monotonically with doping (reflecting average polarization stiffness), $\left|M''_{center}\right|$ fluctuates widely for the 2 wt% sample (0.0015 → 0.0091). As the vertical displacement is geometrically coupled to the depression angle in the Cole–Cole formalism,[64] these fluctuations confirm a physical modification of the relaxation time distribution, mirroring the transient trapping–detrapping events. The use of the electric modulus formalism, combined with the concentration-dependent displacement of the Nyquist semicircle center, effectively suppresses electrode polarization artifacts and supports an intrinsic interfacial origin of the low-frequency response.

In summary, the Nyquist topology confirms the multiscale impact of BQ: (i) intrinsic mobility dominates the pure host; (ii) moderate doping (1 wt%) introduces initial blocking effects; (iii) high doping (2 wt%) generates strong local heterogeneities and interfacial blocking. These observations correlate quantitatively with the activation energies derived in the previous section, confirming the decoupling between fast electronic hopping and slow molecular reorientation.

5.10 Discussion: BQ as a benchmark dopant for soft dielectric engineering

A direct comparison with strong electron acceptors (TCNQ, anthraquinones) provides important context. While such dopants maximize CT interactions, they typically impose a severe structural penalty. TCNQ, for example, tends to disrupt the nematic arrangement, driving a hard transition toward columnar packing *via* dominant π-stacking interactions.[9,11,12] Electrically, the high ionic background inherent to these

systems generates electrohydrodynamic turbulence instead of controlled relaxation,[65] effectively precluding their deployment in stable capacitive architectures. BQ avoids these pitfalls. It operates as a milder, structurally non-destructive agent, allowing us to tailor CT and dielectric properties while preserving the nematic framework. We collate the pivotal dielectric parameters at 323 K in Table 6, which numerically tracks the crossover between these mechanistic regimes.

1. **Energetic Optimization (1 wt% BQ).** At this concentration, BQ lowers the activation barrier for dipolar relaxation to its minimum ($E_a \approx 0.025$ eV). Although the characteristic relaxation time is longer than in the undoped host (1.9×10^{-4} s *vs.* 5.4×10^{-5} s), this regime facilitates charge mobilization at a lower energetic cost. The Nyquist semicircle radius increases moderately ($R_{Nyquist} \sim 0.16$), signaling the onset of mild interfacial constraints rather than severe blocking. Overall, BQ behaves as an energetic modulator, reducing local potential barriers while preserving the global nematic alignment despite modest steric slowing.

2. **Aggregation and interfacial blocking (2 wt% BQ).** At higher doping, the activation energy partially rises (~ 0.035 eV) and the relaxation slows further ($\tau \simeq 2.4 \times 10^{-4}$ s). The Nyquist semicircle expands significantly ($R_{Nyquist} \sim 0.34$), indicating substantial obstruction of conduction pathways (Fig. 17). The non-Debye depression angle θ no longer evolves smoothly; instead, it exhibits temperature-dependent fluctuations (Fig. 18). We interpret this behavior as a signature of defect-mediated transport across a rugged energy landscape.[60] Physically, BQ aggregates act as micro-capacitive interfacial domains, promoting partial charge entrapment and MWS polarization.[42,61] The displacement of the Nyquist semicircle center (Fig. 19) is consistent with the emergence of dynamic heterogeneity.

3. **Intrinsic mobility (pristine host).** The undoped system exhibits the fastest relaxation ($\tau \simeq 5.4 \times 10^{-5}$ s) but is associated with a higher activation barrier. Here, molecular mobility is governed primarily by the intrinsic nematic potential, without dopant-induced modulation.

Conclusion on the doping window. These results identify a critical operational window near 1 wt% BQ. In this regime, CT interactions minimize the activation energy (E_a), providing improved energetic efficiency at the cost of a modest kinetic

Table 6 Summary of BQ doping effects on dielectric relaxation at 323 K. Activation energies E_a (from M''_{max}) show an energetic optimum at 1 wt%, while the relaxation time τ reflects a progressive slowing of dynamics due to complexation and aggregation. Nyquist semicircle radius $R_{Nyquist}$ is measured from M'' *vs.* M' plots

BQ (wt%)	E_a (eV)	τ (s)	$R_{Nyquist}$ (a.u.)
0	~0.040	5.4×10^{-5}	0.06–0.09
1	~0.025	1.9×10^{-4}	0.12–0.16
2	~0.035	2.4×10^{-4}	0.27–0.34

slowdown. Above this concentration, aggregation-driven disorder progressively degrades the dielectric response. BQ therefore appears as a promising, structurally compatible dopant for soft dielectric engineering, offering a tunable means to modulate the activation landscape of nematic fluids.

6 Conclusions

This study presents a systematic multiscale investigation of the dielectric properties of NLCs doped with BQ. By combining calorimetry, optical spectroscopy, and broadband IS analyzed within the electric modulus formalism, we have successfully disentangled the intrinsic relaxation dynamics from electrode polarization artifacts, providing a clear picture of the dopant-host interactions.

Our results establish BQ as a tunable molecular modulator of the M4 nematic host, revealing a concentration-dependent crossover between two distinct mechanistic regimes. At low doping (1 wt%), BQ acts as an energetic modulator. It promotes CT interactions that significantly lower the activation barrier for hopping conduction (~ 0.025 eV). Although this complexation induces a slight kinetic slowing of the relaxation time due to steric effects, this regime optimizes the dielectric response by minimizing energetic losses while preserving the integrity of the long-range nematic order.

In contrast, at higher doping (2 wt%), the system transitions to a disorder-dominated regime. Dopant aggregation leads to the formation of π-stacked clusters that act as deep traps and blocking micro-capacitors. This triggers MWS interfacial polarization, broadens the thermal transitions, and hinders long-range transport, thereby degrading the overall performance. Crucially, the crossover observed in both relaxation dynamics and optical texture near 333 K strongly suggests the thermal instability of these aggregates. A major outcome of this analysis is the identification of a dynamical decoupling between fast electronic charge transport (governed by low-barrier hopping) and slow molecular reorientation (governed by isomerization barriers ~ 0.7 eV). BQ doping enables selective tuning of the electronic properties while preserving the mesophase's structural identity.

Ultimately, we establish BQ as a prototype soft molecular dopant, in contrast to stronger acceptors such as TCNQ that frequently force phase collapse or trigger electrohydrodynamic turbulence. Because it preserves structural integrity, this strategy grants engineers a flexible blueprint for crafting frequency-agile soft matter. Such capability directly opens routes toward low-power electro-optic switches, tunable capacitors, and adaptive energy storage architectures.

Author contributions

Yosr Turki: writing – original draft preparation, supervision, visualization, validation, methodology, investigation, formal analysis, conceptualization, data curation. Bochra Bejaoui: visualization. Ali Benali: writing – review & editing, visualization, validation, supervision, conceptualization. Mohamed Mastouri: resources. Noureddine Raouafi: resources, conceptualization. Youssef Arfaoui: resources, conceptualization.

Conflicts of interest

The authors declare that they have no known competing financial interests or personal relationships that could have appeared to influence the work reported in this paper.

Data availability

All data generated or analyzed during this study are included in this published article. Raw datasets generated during the current study are available from the corresponding author on reasonable request.

Supplementary information (SI) containing additional frequency-dependent spectra for real impedance, complex permittivity, electric modulus, dielectric loss tangent, and Nyquist plots. See DOI: https://doi.org/10.1039/d5ma01481f.

Acknowledgements

Notes and references

1 S. Pieraccini, S. Masiero, A. Ferrarini and G. Piero Spada, *Chem. Soc. Rev.*, 2011, **40**, 258–271.
2 J. C. Jones, *Liq. Cryst. Today*, 2018, **27**, 44–70.
3 I. Dierking and S. Al-Zangana, *Nanomaterials*, 2017, **7**, 305.
4 S. Candau, P. Martinoty and R. Zana, *J. Phys. Lett.*, 1975, **36**, 13–15.
5 W. H. De Jeu, *Mol. Cryst. Liq. Cryst.*, 1981, **63**, 83–109.
6 J. W. van Dijk, W. W. Beens and W. H. de Jeu, *J. Chem. Phys.*, 1983, **79**, 3888–3892.
7 D. Aronzon, E. P. Levy, P. J. Collings, A. Chanishvili, G. Chilaya and G. Petriashvili, *Liq. Cryst.*, 2007, **34**, 707–718.
8 P. S. Guin, S. Das and P. C. Mandal, *Int. J. Electrochem.*, 2011, **2011**, 1–22.
9 A. E. Murschell, W. H. Kan, V. Thangadurai and T. C. Sutherland, *Phys. Chem. Chem. Phys.*, 2012, **14**, 4626.
10 S. Tamaki, Y. Mutoh and K. Isoda, *J. Mol. Liq.*, 2021, **338**, 116636.
11 T. Wöhrle, I. Wurzbach, J. Kirres, A. Kostidou, N. Kapernaum, J. Litterscheidt, J. C. Haenle, P. Staffeld, A. Baro, F. Giesselmann and S. Laschat, *Chem. Rev.*, 2015, **116**, 1139–1241.
12 H. Iguchi, H. Furutani and N. Kimizuka, *Front. Chem.*, 2021, **9**, 657246.
13 P. L. Norcott, *J. Am. Chem. Soc.*, 2023, **145**, 9970–9975.

14 R. Balachandran, V. P. Panov, J. K. Vij, G. Shanker, C. Tschierske, K. Merkel and A. Kocot, *Phys. Rev. E: Stat., Nonlinear, Soft Matter Phys.*, 2014, **90**, 032506.

15 W. H. de Jeu, *Physical properties of liquid crystalline materials*, Gordon and Breach, New York, 1980.

16 S. V. Rosokha and J. K. Kochi, *Acc. Chem. Res.*, 2008, **41**, 641–653.

17 P. R. Bangal, *Chem. Phys. Lett.*, 2005, **401**, 200–204.

18 NIST, Chemistry WebBook, SRD 69, https://webbook.nist.gov/cgi/cbook.cgi?ID=C106514, 2023, accessed Feb 2026.

19 M. E. Orazem and B. Tribollet, *Electrochemical Impedance Spectroscopy*, John Wiley & Sons, Hoboken, 2nd edn, 2017.

20 A. Guerrero, J. Bisquert and G. Garcia-Belmonte, *Chem. Rev.*, 2021, **121**, 14430–14484.

21 W. H. de Jeu and T. W. Lathouwers, *Z. Naturforsch., A*, 1974, **29**, 905–911.

22 P.-G. de Gennes and J. Prost, *The Physics of Liquid Crystals*, Oxford University Press, Oxford, 2nd edn, 1993.

23 M. Kasha, H. R. Rawls and M. Ashraf El-Bayoumi, *Pure Appl. Chem.*, 1965, **11**, 371–392.

24 N. J. Hestand and F. C. Spano, *Chem. Rev.*, 2018, **118**, 7069–7163.

25 I. Jelovica Badovinac, N. Orlic, C. Gellini, L. Moroni and P. R. Salvi, *J. Mol. Struct.*, 2009, **924–926**, 62–65.

26 M. M. J. Tecklenburg, D. J. Kosnak, A. Bhatnagar and D. K. Mohanty, *J. Raman Spectrosc.*, 1997, **28**, 755–763.

27 D. Lin-Vien, N. B. Colthup, W. G. Fateley and J. G. Grasselli, *Aromatic and Heteroaromatic Rings*, Academic Press, San Diego, 1991, ch. 17, pp. 277–306.

28 D. L. Isac, E. Rosca, A. Airinei, E. L. Ursu, R. Puf, I. C. Man, A. Neamtu and A. Laaksonen, *Spectrochim. Acta, Part A*, 2025, **332**, 125828.

29 A. K. Schnack-Petersen, M. Pápai and K. B. Møller, *J. Photochem. Photobiol., A*, 2022, **428**, 113869.

30 F. C. Spano, *Acc. Chem. Res.*, 2009, **43**, 429–439.

31 J. T. S. Irvine, D. C. Sinclair and A. R. West, *Adv. Mater.*, 1990, **2**, 132–138.

32 *Impedance Spectroscopy: Theory, Experiment, and Applications*, ed. E. Barsoukov and J. R. Macdonald, John Wiley & Sons, Hoboken, NJ, 2nd edn, 2005.

33 A. K. Jonscher, *J. Phys. C: Solid State Phys.*, 1973, **6**, L235–L239.

34 A. K. Jonscher, *Dielectric Relaxation in Solids*, Chelsea Dielectrics Press, London, 1983.

35 N. G. McCrum, B. E. Read and G. Williams, *Anelastic and Dielectric Effects in Polymeric Solids*, John Wiley & Sons, London, 1967.

36 F. S. Howell, R. A. Bose, P. B. Macedo and C. T. Moynihan, *J. Phys. Chem.*, 1974, **78**, 639–648.

37 J. D. Hoffman, *J. Appl. Polym. Sci.*, 1969, **13**, 397.

38 F. Tian and Y. Ohki, *IEEE Trans. Dielectr. Electr. Insul.*, 2014, **21**, 929–931.

39 M. Wübbenhorst and J. van Turnhout, *J. Non-Cryst. Solids*, 2002, **305**, 40–49.

40 I. Hodge, M. Ingram and A. West, *J. Electroanal. Chem. Interfacial Electrochem.*, 1976, **74**, 125–143.

41 R. Meena and R. S. Dhaka, *Phys. B*, 2024, **690**, 416209.

42 A. Bendahhou, K. Chourti, R. El Bouayadi, S. El Barkany and M. Abou-Salama, *RSC Adv.*, 2020, **10**, 28007–28018.

43 S. Sharma, T. Basu, A. Shahee, K. Singh, N. Lalla and E. Sampathkumaran, *J. Alloys Compd.*, 2016, **663**, 289–294.

44 V. F. Lvovich, *Impedance Spectroscopy: Applications to Electrochemical and Dielectric Phenomena*, John Wiley & Sons, Hoboken, 2012.

45 A. Behera, N. Mohanty, S. Satpathy, B. Behera and P. Nayak, *Open Phys.*, 2014, **12**, 851–861.

46 H. R. Zeller, *Phys. Rev. Lett.*, 1982, **48**, 334–337.

47 S. Murakami, H. Iga and H. Naito, *J. Appl. Phys.*, 1996, **80**, 6396–6400.

48 K. Chandra, K. Prasad and R. Gupta, *Phys. B*, 2007, **388**, 118–123.

49 H. Bässler, *Phys. Status Solidi B*, 1993, **175**, 15–56.

50 R. Gerhardt, *J. Phys. Chem. Solids*, 1994, **55**, 1491–1506.

51 M. Schadt, *Mol. Cryst. Liq. Cryst.*, 1981, **66**, 319–336.

52 R. Bergman, *J. Appl. Phys.*, 2000, **88**, 1356–1365.

53 R. Kohlrausch, *Ann. Phys.*, 1854, **167**, 179–214.

54 G. Williams and D. C. Watts, *Trans. Faraday Soc.*, 1970, **66**, 80.

55 J. Hobbs, M. Reynolds, M. Krishnappa Srinatha, G. Shanker, J. Mattsson and M. Nagaraj, *J. Mol. Liq.*, 2023, **391**, 123069.

56 S. P. Sreenilayam, N. Yadav, Y. P. Panarin, G. Shanker and J. K. Vij, *J. Mol. Liq.*, 2022, **351**, 118632.

57 S. Sinha, S. K. Chatterjee, J. Ghosh and A. K. Meikap, *J. Phys. D: Appl. Phys.*, 2014, **47**, 275301.

58 W. Cao, *Solid State Ionics*, 1990, **42**, 213–221.

59 D. L. Sidebottom, P. F. Green and R. K. Brow, *Phys. Rev. Lett.*, 1995, **74**, 5068–5071.

60 J. C. Dyre, *J. Appl. Phys.*, 1988, **64**, 2456–2468.

61 in *Broadband Dielectric Spectroscopy*, ed. F. Kremer and A. Schönhals, Springer, Berlin, Heidelberg, 2003.

62 L. Berthier and G. Biroli, *Rev. Mod. Phys.*, 2011, **83**, 587–645.

63 in *Dynamical Heterogeneities in Glasses, Colloids, and Granular Media*, ed. L. Berthier, G. Biroli, J.-P. Bouchaud, L. Cipelletti and W. van Saarloos, Oxford University Press, Oxford, 2011.

64 K. S. Cole and R. H. Cole, *J. Chem. Phys.*, 1941, **9**, 341–351.

65 A. Baise, I. Teucher and M. Labes, *Appl. Phys. Lett.*, 1972, **21**, 142–143.